XDEM - FEM Coupling Simulations of the Interactions between a Tire Tread and Granular Terrain

Mark Michael[a,*], Frank Vogel[b], Bernhard Peters[a]

[a] *FSTC, University of Luxembourg, L-1359 Luxembourg*
[b] *inuTech GmbH, Frther Strae 212, 90429 Nuremberg, Germany*

Abstract

This study proposes an efficient combination of the Discrete Element Method (DEM) and the Finite Element Method (FEM) to study the tractive performance of a rubber tire in interaction with granular terrain. The presented approach is relevant to all engineering devices interacting with granular matter which causes response forces.

Herein, the extended discrete element method (XDEM) is used to describe the dynamics of the granular assembly. On the one hand, the discrete approach accounts for the motion and forces of each grain individually. On the other hand, the finite element method accurately predicts the deformations and stresses acting within the tire tread. Hence, the simulation domain occupied by the tire tread is efficiently described as a continuous entity. The coupling of both methods is based on the interface shared by the two spatially separated domains. Contact forces develop at the interface and propagate into each domain. The coupling method enables to capture both responses simultaneously and allows to sufficiently resolve the different length scales. Each grain in contact with the surface of the tire tread generates a contact force which it reacts on repulsively. The contact forces sum up over the tread surface and cause the tire tread to deform. The coupling method compensates quite naturally the shortages of both numerical methods. It further employs a fast contact detection algorithm to save valuable computation time.

The proposed DEM-FEM Coupling technique was employed to study the tractive performance of a rubber tire with lug tread patterns in a soil bed. The contact forces at the tread surface are captured by 3D simulations for a tire slip of $s_T = 5\%$. The simulations showed to accurately recapture the gross tractive effort T_H, running resistance T_R and drawbar pull T_P of the tire tread in comparison to related measurements. Further, the traction mechanisms between the tire tread and the granular ground are studied by analysing the motion of the soil grains and the deformation of the tread.

Keywords: Tire Tread, Soil, Traction, DEM - FEM Coupling, Finite Element Method (FEM), eXtended Discrete Element Method (XDEM)

1. Introduction

A broad range of engineering applications faces multi-scale problems. A large number of these problems involve heterogeneous materials such as granular media. Applications in fracture mechanics, soil-structure interaction, fluidized particle beds and tire-terrain interaction are major fields to name a few when it comes to dealing with different length scales.
The combination of discrete and continuum approaches (CCDM - Combined Continuum and Discrete Model) is a powerful tool to account for different scales within problems.
Traditional numerical methods, such as the Finite Element Method (FEM), describe materials as continuous entities. This assumption allows an increasing number of engineering problems to be solved conveniently at the macroscopic scale. But this approach inherits one fundamental drawback the averaging of all individual characteristics of the grain scale.
However, high performance computer technique now enables the employment of methods, such as the Discrete Element Method (DEM), able to account for the individual behaviour of each grain within a granular assembly. This allows to derive the macroscopic char-

*Universit du Luxembourg, Facult des Sciences de la Technologie et de la Communication, Campus Kirchberg, 6 rue Coudenhove-Kalergi, L-1359 Luxembourg, (+352) 46 66 44 58 13, contact@markmichael.eu

acteristics from the behaviour observed at each single grain. But since the discrete approach requires for contact detection, calculation of all contact reactions and a high resolution of the time scale, the method inherits large computation time as a significant disadvantage.
Hence, the idea seems quite natural to utilize the advantages of both the continuum and the discrete approach and thereby compensating the shortages of each method. The field of coupling between continuum and discrete methods can be separated into two parts, methods with overlapping and methods with separated physical domains. Applications with overlapping domains are computations of the fracture and fragmentation of materials and structures, multiscale problems of heterogeneous materials, hypervelocity impacts on structures, fluid - solid interaction, as applied by Morris et al. (2006), Nitka et al. (2009), Beissel et al. (2006) and Idelsohn et al. (2006), respectively. However, in the field of coupling methods with non-overlapping domains major contribution evolve from the research field of fluid flows with solid parts, as investigated by Tsuji et al. (1993) and Xu and Yu (1998). Further, valuable effort comes from the field of soil mechanics and terramechanics where soil structures have to be reinforced, see Villard et al. (2009). Non-overlapping applications with a more dynamical interaction come from vehicle - soil or tire - terrain interaction as investigated in this study and by Nakashima and Oida (2004), Nakashima et al. (2009) and Horner et al. (2001).
The purpose of the computation of tire - terrain interaction is the study of the traction mechanisms between the tread and the granular ground. The traction force is not only the integral force of the friction of each individual grain in contact with the tire surface. The traction is also influenced by interlocking mechanisms between tread parts and the granular material.

2. Extended Discrete Element Method (XDEM)

The Lagrangian Time-Driven Method is applied to each discrete particle of a moving ensemble. The ensemble is thereby defined as a system of a finite number of particles with a distinctive shape and material properties.
The state of the particles is predicted through integration in time of the equations of rigid body motion. Thereby, the timescale is subdivided by the discrete timestep length dt and the state of each particle of the granular ensemble is predicted at every discrete timestep t_i, i.e. position, velocity, orientation and angular velocity,. Newton's second law for translation and rotation of each particle in the ensemble is integrated over time. Therefore, all forces and torques acting on each particle need to determined at every timestep.

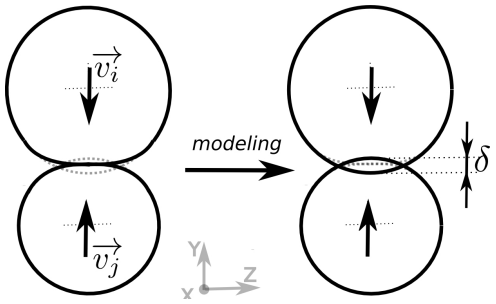

Figure 1: Particle deformations modeled by overlap

Two bodies colliding experience small deformations which causes stress to develop at the contacting surface. However, the deformations between two colliding gains are modelled by means of an overlap δ between the two geometrical shapes as shown in fig. 1. The developing collision forces are derived from the overlap geometry, material properties and kinematic quantities of the adjoining particles. The collision force developing between a grain and a boundary wall is also modelled based on the overlap δ resulting from the grain geometry and the surface.

2.1. Equations of Rigid Body Motion

In this study, the translation of a rigid body, i.e. discrete particle, is predicted by the explicit integration of Newton's second law. Further, Euler's equation of rotational motion is used to determine the evolution of the orientation of a particle, i.e. grain, over time.

2.1.1. Particle Translation

Particle Forces

The position of a rigid body in space is defined uniquely by the three component vector x_α referring to the three spatial dimensions. The change in position occurs with a forces $\vec{F}_i$ acting on a particle. The force vector $\vec{F}_i$ acting on a particle i is the sum of all collision $\vec{F}_i^c$, gravitational $\vec{F}_i^g$ and external forces $\vec{F}_i^e$ in eq. 1.[1]

$$\vec{F}_i = \vec{F}_i^c + \vec{F}_i^g + \vec{F}_i^e \tag{1}$$

However, the collision force $\vec{F}_i^c$ of a particle i is the sum of all collision forces $\vec{F}_{ij}^c$ generated while colliding

[1]The roman indices i, j, k identify the i^{th} particle out of n, i.e. $i = (1, 2, ..., n)$

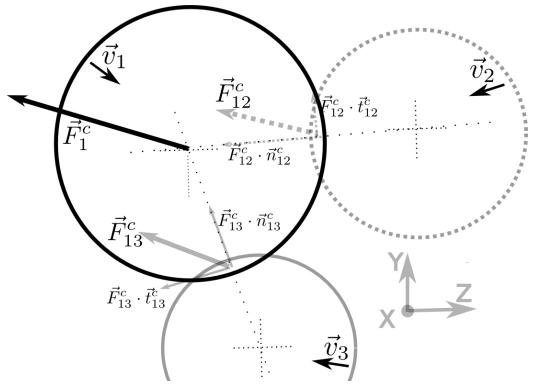

Figure 2: Particle force due to colliding with particle 2 and 3

with the neighbouring bodies j. This is mathematical described by eq. 2 where n is the number of neighbouring particles in contact and boundary shapes interacting with the particle i, as shown in fig. 2.

$$\vec{F}^c_i = \sum_{j=1, j\neq i}^{n} \vec{F}^c_{ij} \tag{2}$$

At the point of collision, each collision force $\vec{F}^c_{ij}$ is composed of a tangential $\vec{F}^{c,t}_{ij}$ and normal component $\vec{F}^{c,n}_{ij}$. The normal unit vector $\vec{n}^c_{ij}$ points from the center of the particle j to the center of i with the tangential direction $\vec{t}^c_{ij}$ orthogonal to $\vec{n}^c_{ij}$.

Time Integration of the Particle Position

The translation of a rigid body, i.e. discrete particle, is described by Newton's second law. Newton's well-known equation 3 relates to the kinematic quantities at the center of gravity of a particle i as follows:

$$\frac{d\vec{x}_i^{\,2}}{dt^2} = \frac{d\vec{v}_i}{dt} = \vec{a}_i = \frac{\vec{F}_i}{m_i} \tag{3}$$

where m_i denotes the particle mass, $\vec{v}_i$ the velocity, $\vec{a}_i$ acceleration, $\vec{x}_i$ center of gravity and $\vec{F}_i$ the force acting on the particle.
Consequently with the summation of all forces acting on a particle, Newton's second law in eq. 3 is used to obtain the new particle acceleration which can be expressed by $\ddot{x} \longrightarrow \dot{x} \longrightarrow x$. To further follow the evolution of a granular ensemble, the new position $\vec{x}_i^{\,t+dt}$ and new velocity $\vec{v}_i^{\,t+dt}$ of every particle are computed by numerical integration over every discrete time dt between t and $t + dt$. From the investigations of Samiei (2012), this study draws the conclusion to employ the Velocity Verlet method to predict the new particle states. The Velocity Verlet showed the best balance between accuracy and computational effort in relation to the snow simulations ahead. The method proposed by the French physicist Loup Verlet can be derived by an approximation of a Taylor series. The basic Verlet method makes use of a central difference approximation, where the new particle position $\vec{x}_i^{\,t+dt}$ is predict as follows:

$$\vec{x}_i^{\,t+dt} = \vec{x}_i^{\,t} + \vec{v}_i^{\,t} dt + \frac{1}{2}\vec{a}_i^{\,t} \cdot dt^2 \tag{4}$$

The new particle velocity $\vec{v}_i^{\,t+dt}$ is determined as follows:

$$\vec{v}_i^{\,t+dt} = \vec{v}_i^{\,t} + \frac{1}{2}(\vec{a}_i^{\,t} + \vec{a}_i^{\,t+dt})dt \tag{5}$$

where $\vec{a}_i^{\,t}$ is the sum of all current and $\vec{a}_i^{\,t+dt}$ is the sum of all new forces. Concerning the implementation, this approach does not allocate additional memory as the prediction of the new velocity is split into a predictor and corrector phase of the procedure. In detail this means that the current acceleration $\vec{a}_i^{\,t-dt}$ is determined and added on the new velocity ahead of the prediction of the new forces. After the prediction of the new forces the new velocity is corrected by adding the new acceleration.

2.1.2. Particle Rotation

Notation

The orientation of a rigid body in space can be defined by the three Euler angles ϕ_α. The change of orientation occurs with a torque $\vec{M}_i$ acting on a particle. A change in orientation causes a new state of the Euler angles, hence, the angles present a sequence of three rotations about the axes of the reference system. By definition within XDEM, the first rotation is about X^S_3 by the angle ϕ_1, the second about X'^S_1 by the angle ϕ_2 and the final rotation is again around X''^S_3 but by the angle ϕ_3.
However, the new orientation, i.e. the new Euler angles, can be derived in all three spatial dimensions from the total torque $\vec{M}_i$ that acts on a particle. But this inherits somehow more complexity compared to translational motion. Therefore, three different co-coordinate systems have be defined for the evolution of the new orientation which are the space-fixed coordinate system $\vec{X}_S$, the co-moving coordinate system $\vec{X}_C$ and the body-fixed coordinates $\vec{X}_B$.

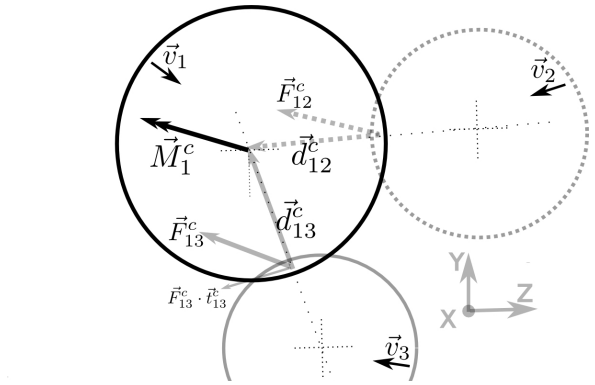

Figure 3: Particle torque during collision with two neighbours

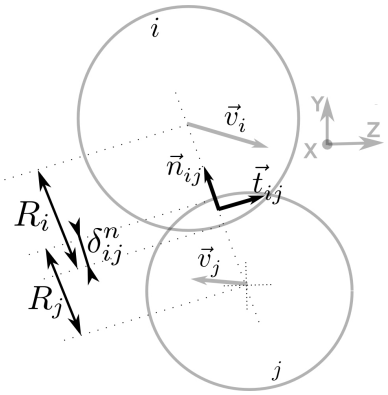

Figure 4: Contact configuration and normal overlap of grain i and j

Particle Torques

The total torque $\vec{M}_i$ on a particle i is composed of collision $\vec{M}^c_i$ and external moments $\vec{M}^e_i$ as follows:

$$\vec{M}_i = \vec{M}^c_i + \vec{M}^e_i \tag{6}$$

The torque $\vec{M}^c_i$ on a particle i developed during a collision is the sum of all the forces $\vec{F}^c_{ij}$ acting at the collision point times the relative distance $\vec{d}^c_{ij}$ to center of mass of the particle:

$$\vec{M}^c_i \;=\; \sum_{j=1, j\neq i}^{n} \vec{M}^c_{ij} \;=\; \sum_{j=1, j\neq i}^{n} \vec{d}^c_{ij} \times \vec{F}^c_{ij} \tag{7}$$

The mathematical formulation of eq. 7 is illustrated accordingly in fig. 3.

Time Integration of the Particle Orientation

In XDEM, the Euler equation of rotational motion is applied to predict a change of the particle orientation, which can be written as follows:

$$\begin{bmatrix} M^B_1 \\ M^B_2 \\ M^B_3 \end{bmatrix} = \begin{bmatrix} I_{11}\dot{\omega}^B_1 - \omega^B_2\omega^B_3(I_{22} - I_{33}) \\ I_{22}\dot{\omega}^B_2 - \omega^B_3\omega^B_1(I_{33} - I_{11}) \\ I_{33}\dot{\omega}^B_3 - \omega^B_1\omega^B_2(I_{11} - I_{22}) \end{bmatrix} \tag{8}$$

where $\vec{M}^B$ and $\vec{\omega}^B$ describe the torque and the angular velocity of the bodies in the body-fixed coordinate system, respectively. To make use of the moment of inertia $I_{\alpha\beta}$ in the principal directions, i.e. I_{11}, I_{22} and I_{33}, of a shape the torque in eq. 8 has to be transformed into body-fixed coordinates. The three equations are solved for the three unknown angular velocities ω^B_α of a particle.[2] Thereafter, the change in Euler angles $\dot{\phi}_\alpha$ is predicted by making use of the relations in Eqs. 9.

$$\begin{bmatrix} \dot{\phi}_1 \\ \dot{\phi}_2 \\ \dot{\phi}_3 \end{bmatrix} = \begin{bmatrix} \dfrac{\omega^B_x \sin\phi_3 + \omega^B_y \cos\phi_3}{\sin\phi_2} \\ \omega^B_x \cos\phi_3 - \omega^B_y \sin\phi_3 \\ \omega^B_z - (\omega^B_x \sin\phi_3 + \omega^B_y \cos\phi_3)\dfrac{\cos\phi_2}{\sin\phi_2} \end{bmatrix} \tag{9}$$

Finally, the angular velocities is transformed back into space-fixed coordinates as this is the reference system.

2.2. Model of Grain Collision

2.2.1. Contact Properties

The forces and torques developing between colliding grains are estimated from the contact properties at the point of contact. The properties are described within the local contact frame which is defined by the normal $\vec{n}_{ij}$ and tangential $\vec{t}_{ij}$ unit vector at the contact point, as show in fig. 4. The normal direction $\vec{n}_{ij}$ of a contact is given by eq. 10 and points always from grain j to grain i.

$$\vec{n}_{ij} \;=\; \frac{\vec{x}_i - \vec{x}_j}{\left|\vec{x}_i - \vec{x}_j\right|} \tag{10}$$

Having the normal direction estimated the location of the point of contact $\vec{x^c}_{ij}$ itself is given by eq. 11.

$$\vec{x^c}_{ij} \;=\; \vec{x}_i + \vec{n}_{ij} \cdot (r_j - \left|\vec{x}_i - \vec{x}_j\right|) \tag{11}$$

The velocity $\vec{v}_{ij}$ at the contact point is predicted by eq. 12 taking into account the angular and translational velocities of the contacting particles, as shown in fig. 5.

$$\vec{v}_{ij} \;=\; (\vec{\omega}_i \times \vec{d}^c_{ij} + \vec{v}_i) - (\vec{\omega}_j \times \vec{d}^c_{ji} + \vec{v}_j) \tag{12}$$

The normal and tangential velocity, $\vec{v^n}_{ij}$ and $\vec{v^t}_{ij}$ respectively, at the point of contact are defined as:

$$\vec{v^n}_{ij} \;=\; (\vec{v}_{ij} \cdot \vec{n}_{ij}) \cdot \vec{n}_{ij} \tag{13}$$

[2] The Greek indices $_\alpha$, $_\beta$, $_\gamma$ identify the three spatial components of a quantity.

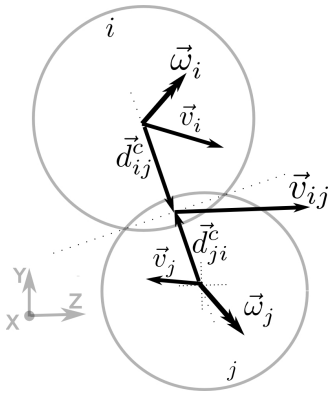

Figure 5: Velocity at the point of contact

$$\vec{v^t}_{ij} = \vec{v}_{ij} - \vec{v^n}_{ij} \tag{14}$$

The tangential direction $\vec{t}_{ij}$ of the contact configuration is defined as the direction of the tangential velocity at the contact point by eq. 15.

$$\vec{t}_{ij} = \frac{\vec{v^t}_{ij}}{\left|\vec{v^t}_{ij}\right|} \tag{15}$$

The effective radius R_{ij} and reduced mass m_{ij} of two grains in contact are determined according to the theory of Hertz (1881) by eq. 16 and eq. 17, respectively.

$$\frac{1}{R_{ij}} = \frac{1}{r_i} + \frac{1}{r_j} \tag{16}$$

$$\frac{1}{m_{ij}} = \frac{1}{m_i} + \frac{1}{m_j} \tag{17}$$

The characteristics of a collision are the duration of a contact t_c, the normal δ^n_{ij} and tangential overlap δ^t_{ij} and the relative velocity $\vec{v}_{ij}$ at the point of contact. Here, the normal overlap δ^n_{ij} represents the deformations of the grains in normal direction. As deformation causes stress, the normal overlap is finally used to estimated the resulting normal force $\vec{F}^{c,n}_{ij}$. Hence, the tangential overlap represents the deformation of the asperities at the grain surface. Therefore, the tangential overlap is employed to predict the frictional force $\vec{F}^{c,n}_{ij}$ in tangential direction.
Eq.18 evaluates the normal overlap δ^n_{ij} with the radii r_i and r_j of the spherical particles and is presented in fig. 4.

$$\delta^n_{ij} = r_i + r_j - \left|\vec{x}_i - \vec{x}_j\right| \tag{18}$$

The duration of a collision t_c is defined as the time for which normal overlap is existing continuously. The collision time is estimated as follows:

$$t_c = t - t^c_0 = i_c \cdot dt \tag{19}$$

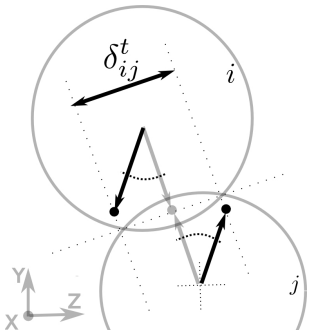

Figure 6: Tangential overlap of grain i and j

where t denotes either the end time of the contact or the current time, t^c_0 denotes the start time of the contact and i_c the total number of time steps in contact. The number of time steps of a contact is given by $i_c = t_c/dt$. As to be seen in fig. 6, the tangential overlap derives from the relative tangential path taken by the point of contact over the entire time spent in a collision. Therefore, the tangential overlap δ^t_{ij} is calculated as follows:

$$\begin{aligned} \delta^t_{ij}(t) &= \left|\vec{\delta}^t_{ij}(t)\right| \\ \vec{\delta}^t_{ij}(t) &= \sum_{i=1}^{i_c} \vec{v^t}_{ij}\left(t^c_0 + i \cdot dt\right) \cdot dt \end{aligned} \tag{20}$$

where t equals the current time step, t^c_0 the start time of the contact and i_c the total number of time steps during a contact. Thus eq. 20 predicts δ^t_{ij} as the sum of all tangential velocities over the contact time.
The effective Young's modulus E_{ij} at the interface of two colliding grains is predicted according to Hertz (1881) given by:

$$\frac{1}{E_{ij}} = \frac{1-\nu_1^2}{E_i} + \frac{1-\nu_2^2}{E_j} \tag{21}$$

2.2.2. Hertz-Mindlin Collision Model

The Hertz-Mindlin model is based on the theory of Hertz (1881). The normal elastic force and the normal energy dissipation are modeled based on the theory proposed by Mindlin (1949). The formula for the normal force can be written as follows:

$$\vec{F}^{c,n}_{ij} = -\left(\frac{4}{3}E_{ij} \cdot \sqrt{R_{ij}} \cdot \left(\delta^n_{ij}\right)^{\frac{3}{2}} + c_n \cdot \left(\delta^n_{ij}\right)^{\frac{1}{4}} \cdot \dot{\delta}^n_{ij}\right) \cdot \vec{n}_{ij} \tag{22}$$

The equation for the normal dissipation coefficient c_n is proposed by Tsuji et al. (1992) as follows:

$$\begin{aligned} c_n = \ln e \cdot \sqrt{\frac{5 \cdot m_{ij} \cdot k_n}{\pi^2 + \ln e^2}} \qquad &\text{with} \\ k_n = \frac{4}{3} \cdot E_{ij} \cdot \sqrt{R_{ij}} & \end{aligned} \tag{23}$$

The tangential force is a function of static and dynamic friction whereby the static friction is model by a spring-dashpot model:

$$\vec{F}_{ij}^{c,t} = min\left[\left(k_t \cdot \delta_{ij}^t + c_t \cdot \dot{\delta}_{ij}^t\right) \cdot \vec{t}_{ij} \;\; ; \;\; \mu \cdot \vec{F}_{ij}^{c,n} \right] \quad (24)$$

where δ_{ij}^t is the tangential spring displacement which is defined as the total displacement in the tangential direction since the beginning of this contact. The tangential stiffness is estimated by eq. 25.

$$k_t = 8 \cdot G_{ij} \cdot \sqrt{R_{ij} \cdot \delta_{ij}^n} \quad (25)$$

where G_{ij} is the effective shear modulus defined in eq. 26.

$$\frac{1}{G_{ij}} = \frac{2-\nu_i}{G_i} + \frac{2-\nu_j}{G_j} \quad (26)$$

The tangential dissipation coefficient is derived from the tangential stiffness using eq. 27.

$$c_t = \ln e \sqrt{\frac{5 \cdot (4 \cdot m_{ij} \cdot k_t)}{6 \cdot (\pi^2 + \ln e^2)}} \quad (27)$$

3. Finite Element Method (FEM)

The tire tread investigated in this study is described as a continuous body. The displacement or change of the configuration of a continuous body is the sum of motion, i.e. translation and rotation, and the deformation of its shape. Thereby, the deformational part reflects the stresses acting inside the body. A configuration of a continuum body describes a continuous number of material points occupying a certain amount of space at a particular time. Deformation, i.e. the change of shape or size of the body, equals the change between the initial and the current configuration. The deformation can thereby described as the change in distance between two neighbouring material points between initial and current configuration. To analyse the evolution of deformation of a continuous body it is necessary to describe the change of configurations throughout time. Therefore, the method discretized the volume of a body by means of a mesh, as exemplified in fig. 7. This mesh is represented by a finite number of nodes spanning a finite number element over the body volume. The displacements of the body shape are predicted at the mesh nodes and thus the deformations and stresses are derived over the finite elements.

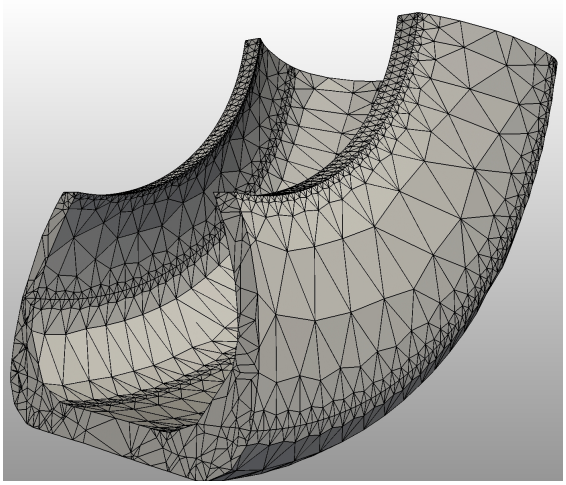

Figure 7: Finite element mesh of a portion of a tire tread.

3.1. Elastic Body Deformation

In this study, the investigated tire tread is described by a fully time dependent model of linear elastic deformation. The deformation of an elastic continua is described by the differential form of Newton's second law of eq. 28. [3] Contrary to the discrete approach this equation is valid in every volume point of the continuum.

$$\rho \frac{\partial u_\alpha^2}{\partial t^2} = \frac{\partial \sigma_{\alpha\beta}}{\partial x_\beta} + \rho\, b_\alpha \quad (28)$$

Notice within this context u_α describes the displacement where in the discrete form the position $\vec{x}_i$ is placed. In eq. 28, ρ is the density, $\sigma_{\alpha\beta}$ reflects the internal forces due to stresses and the final term represents body forces $\vec{b}$. As the density and body forces are prescribed, six unknowns remain within the symmetric stress tensor by three equations. To yield closure of the system the stresses and deformations are linked by Hooke's generalized elastic law which can be written as follows:

$$\sigma_{\alpha\beta} = \lambda \frac{\partial u_\gamma}{\partial x_\gamma} \delta_{\alpha\beta} + \mu \left(\frac{\partial u_\alpha}{\partial x_\beta} + \frac{\partial u_\beta}{\partial x_\alpha} \right) \quad (29)$$

where $\sigma_{\alpha\beta}$ describes the stresses, λ and μ are the Lame's linear elastic parameter.In this section $\delta_{\alpha\beta}$ describes the Kronecker symbol. The law describes the isotropic linear elasticity.

[3] The Greek indices α, β, γ identify the three spatial components of a physical quantity, i.e. $\alpha = (1, 2, 3)$

3.2. The Finite Element Formulation

The discretization of the governing eq. 28 in time is described by a three-point central difference scheme. The scheme is employed by introducing the superscript t reflecting the time level and can be written as follows:

$$\rho \frac{u_\alpha^{t-dt} - 2u_\alpha^t + u_\alpha^{t+dt}}{dt^2} = \frac{\partial \sigma_{\alpha\beta}^t}{\partial x_\beta} + \rho\, b_\alpha^t \tag{30}$$

where all quantities superscripted with t are time dependent and dt sets the time step length. For the spatial approximation the straightforward Galerkin method is applied to the governing eq. 28. Thereby, the displacement field is approximated at n discrete nodal points of finite element mesh as follows:

$$\hat{u}_\alpha = \sum_{j=1}^{n} u_j^\alpha \cdot N_j(x_\alpha) \tag{31}$$

where N_j are trial functions of the finite element and u_j^α contains $n \cdot 3$ unknowns to predict, where 3 stands for the three spatial dimensions.
As the Galerkin method inserts the approximation $\hat{u}_\alpha$ for u_α a residual results. By multiplication with the trial function the resulting residual is required to vanish.
The final discretized form of the governing eq. 28 to compute isotropic elastic deformation can be written:

$$\mathbf{u}^{t+dt} = 2\mathbf{u}^t - \mathbf{u}^{t-dt} + \mathbf{M}^{-1} dt^2 \cdot \left(-\mathbf{K}\mathbf{u}^t + \mathbf{b}^t\right) \tag{32}$$

where $\mathbf{M} = M_{ij}^{\alpha\beta}$ being the mass matrix of the system. $M_{ij}^{\alpha\beta}$ thereby holds the following entries:

$$M_{ij}^{\alpha\beta} = \int_\Omega \cdot N_i \cdot N_j d\Omega \tag{33}$$

where Ω describes the whole domain of the body and is replaced by the domain Ω_e of the element e, restricting i and j to be nodes of the finite element. Further, $-\mathbf{K}\mathbf{u}^t + \mathbf{b}^t$ is the discretized form of $\sigma_{\alpha\beta,\beta}^t + \rho b_\alpha^t$. $\mathbf{K}$ thereby equals the stiffness matrix of the system with the entries $K_{ij}^{\alpha\beta}$. The stiffness matrix holds thereby the following entires:

$$K_{ij}^{\alpha\beta} = \int_\Omega \Big[\mu \left(N_{i,\gamma} \cdot N_{i,\gamma}\right) \cdot \delta_{\alpha\beta} + \mu \cdot N_{i,\alpha} \cdot N_{j,\beta} + \lambda \cdot N_{i,\beta} \cdot N_{j,\alpha} \Big] d\Omega \tag{34}$$

where i and j run over all nodal points n of the mesh while α, β and γ are presenting the three spatial dimensions (= 1, 2, 3). The term $\mathbf{b}$ holds all nodal forces.

3.3. The Computational Algorithm

Looking at the time-stepping scheme of eq. 32 one notices that it gains the new value $\mathbf{u}^{t+dt}$ just by conducting vector addition, matrix-vector and scalar multiplication. Hence, the scheme is an explicit procedure without a linear equation system to be solved. Eq. 32 is assuming that $\mathbf{u}^t$ and $\mathbf{u}^{t-dt}$ are already predicted. Therefore, the computational algorithm starts at $t = t_0$ by solving the stationary elasticity problem $\mathbf{K}\mathbf{u}^{t_0} = \mathbf{b}^{t_0}$ implicitly before it enters the time loop. Thus, the linear equation system $\mathbf{K}\mathbf{u}^t = \mathbf{b}^t$ needs to be solved ones for $t = t_0$ by an iterative method. The solution provides $\mathbf{u}^{t_0}$. Thereafter, $\mathbf{u}^{t_0}$ and $\mathbf{u}^t$ are equalized which implies the entire system is stationary unless $\mathbf{b}^t$ changes which is a reasonable assumption. While solving eq. 32 at every time step $t_0 + i \cdot dt$, the initial gained stiffness matrix $\mathbf{K}$ of the stationary solution is reused.

3.4. Linear Equation System

By discretizing partial differential equations by the finite element method one mostly needs to solve a system of linear algebraic equations. In this study the C++ libraries of the finite element toolbox DiffPack are utilized to assemble and solve such a system. For that purpose the libraries offer direct and iterative methods and also provide flexible functionality to utilize the specific matrix and vector structure assemble.
The time-stepping scheme of eq. 32 does not require any solving of a linear equation system. However, the initial prediction of the stationary elasticity problem $\mathbf{K}\mathbf{u}^{t_0} = \mathbf{b}^{t_0}$ is a solution of a system of linear algebraic equations. Therefore, the linear equation system $\mathbf{K}\mathbf{u}^{t_0} = \mathbf{b}^{t_0}$ needs to be solved for $n \cdot 3$ unknowns contained in the vector $\mathbf{u}$.
In this study, the Conjugate Gradient Method as an successful iterative method to solve $\mathbf{A} \cdot \mathbf{x} = \mathbf{b}$ linear systems is chosen to do so.

4. Efficient XDEM - FEM Coupling Method

The coupled computation conducted in this study are separated into two domains the Finite Element and the Discrete Element simulations. These two domain stay separated through the entire time loop and integrate their quantities without interfering. Only, at characteristic points within a the time loop necessary data is shared to update each domain.

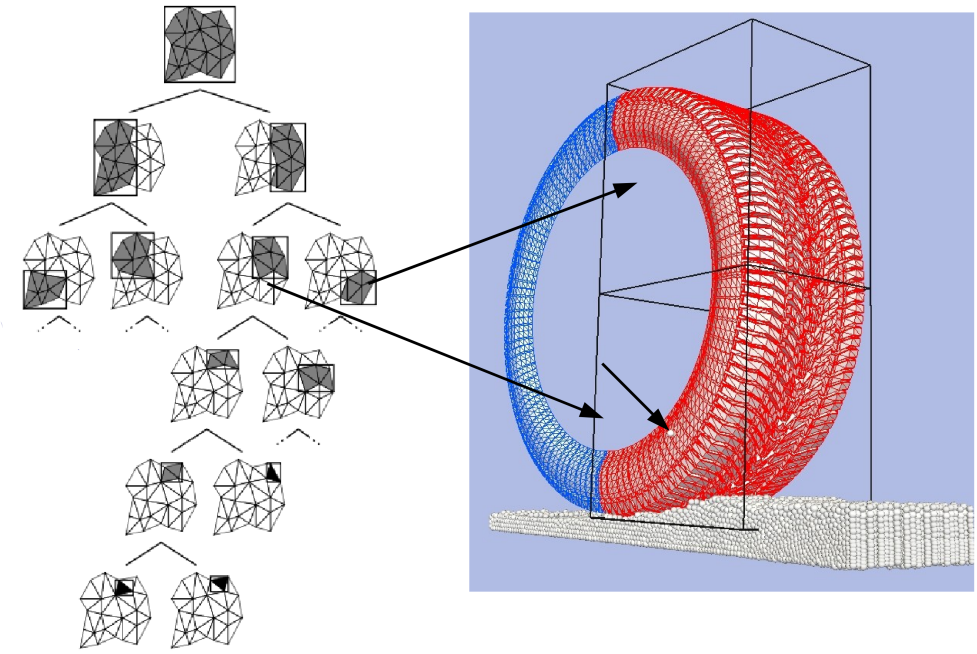

Figure 9: Binary Tree with stored bounding volumes exemplified by a tire tread. The root bounding volume encapsulates the entire surface elements while bottom branch holds a single surface triangle.

4.1. Coupling Procedure

Within the context of explicit time integration the procedure of the DEM - FEM coupling algorithm is relatively straight forward. The procedure is schematically depicted in fig. 8. Before the procedure enters the time loop to predict the motion of particles and the deformation of the solid body, an initiation phase is required to establish the foundation for later information exchange. The surface elements of the mesh of the body have to be linear triangle elements as the efficient contact detection is base on the intersection between spheres and triangles. As depicted in fig. 8 the initiation starts with solving the stationary problem with in the FEM domian. This step provides two informations to the procedure.
First, it established the matrices and initial displacement values for eq. 32 of the FEM domain. On the other hand it serves with the first deformed structure for the DEM domain.
The second step of the initiation phase mirrors the deformed surface elements of the FEM mesh into DEM domain. At any time, the DEM domain sees the deformed surface elements of the finite element mesh as geometrical boundary conditions. On this basis the coupling algorithm is linking the particular surface element with the according boundary shape between FEM and

```
                    Initiation
↦ solve → Ku^0 = b^0
↦ mirror displaced surface elements
      Time Loop → i → t_i = t_0 + i · dt
↦ integrate time step  t_i
  of particle motion, eq. 3  &  8
↦ transfer contact forces
     ↦ predict potential contact pairs
     ↦ compute contact forces
     ↦ interpolate forces onto
       finite element
↦ integrate time step  t_i
  of body deformation, eq. 32
↦ update boundary shapes
```

Figure 8: General Procedure of the Coupling Algorithm

DEM domain respectively.
The loop over time is separated into four major parts. First, the motion of the granular assembly is integrated. This step integrates the position and orientation of particles according to eq. 1 and 9. In the second step, the impacts between particles and the elastic body are predicted. Third, the deformation of elastic body due to the impacting forces can be solved by the FEM scheme. The last part of the procedure updates position of the boundary shapes before the particle motion is re-predicted within the new time step.
In the second step, between the integration of the motion of particles and the integration of the deformation of the elastic body, the contact forces need to be computed and transferred. This step is partitioned into three sub steps.
First the potential contact pairs are detected by means of an efficient contact detection algorithm, which quickly separates the important particle - surface element pairs from the huge number of possible contact pairs within the system. The fundamentals of the algorithm are explained below.
The second sub step computes contact forces for all pairs provided by the contact detection algorithm. The contact force between particle and triangular element is also derived by an representative overlap. The overlap prediction in this particular geometrical case is described in the following sections. However, the contact force is added to the particle forces and the counter force is transfer to the according surface element of the FE mesh.
The third sub step interpolates the counter force onto the nodal forces of the finite element.
In the third step elastic deformation are executed which incorporates the insertion of interpolated contact forces into the force vector b^l of the finite element formulation. Then, the new displacement value $\mathbf{u}^{l+1}$ will be gain by solving eq. (32).
In the final step, each boundary shape within the DEM domain is updated according to the appropriate surface element. Therefore, the position and displacement vector of every nodal point of the surface mesh are added and the appropriate vertex of the triangular boundary shape is equalized with the result.

4.2. Contact Detection

An efficient coupling of discrete and finite elements is based on a fast contact detection. Hence, the coupling and quantity exchanging procedure is based on the information which pairs of particles and elements are in contact. To avoid proofing each pair for contact an algorithm for quick contact detection has been developed. The algorithm is predicated on a binary tree structure storing cubic bounding volumes. Fig. 9 shows a binary tree with bounding volumes stored at every tree level on the example of a tire tread.
The root node is encapsulating all surface elements of the meshed body. By accessing a lower level of the tree the bounding volume of the previous level is split into half by spatial dimensions and number of elements encapsulated. The final branches of the binary tree only hold the reference to a single surface element.
For the prediction of contact pairs the algorithm simply runs along the branches. The algorithm detects whether a particle is within the dimensions of the bounding volume of one of the two child branches. If this is the case the algorithm repeats the detection on the next lower level. As the algorithm reaches a bottom node of the binary tree, the particle and the remaining surface element will be returned a potential contact pair. In any other case the contact detection algorithm restarts with next particle.

4.3. Contact Prediction

For each detected contact pair, particle - triangular finite element, the particular overlap δ_{ij} and point of contact $\vec{x}_{ij}^{\,c}$ are predicted for the contact force computation.
The contact prediction between a sphere and triangle can be separated into three contact situations as depicted in fig. 10. The spherical particle can thereby intersect with the interior, the edges or a vertex of the triangular shape.
By means of the natural coordinates of a linear triangle an efficient and quick prediction of the contact situation is enabled. The natural coordinates can be presented as the portion of area A_i to entire triangle area A_Δ which can be formulated as follows:

$$\zeta_1 = \frac{A_1}{A_\Delta} \quad \zeta_2 = \frac{A_2}{A_\Delta} \quad \zeta_3 = \frac{A_3}{A_\Delta} \tag{35}$$

Thus, any point aligning in the plane of a triangle may be located in terms of natural coordinates ζ_i as illustrated in fig. 11.

4.4. Point Force to Nodal Force

Within the FEM domain impacting particles are recognised as point forces acting on the surface of an element, as illustrated in fig. 12. But the displacement are computed at the nodal points of an element. Hence, the point force has to be interpolated consistently onto the nodes to account for them within the finite element formulation of eq. (32). The force interpolation is based on the virtual work equivalent to secure consistent nodal

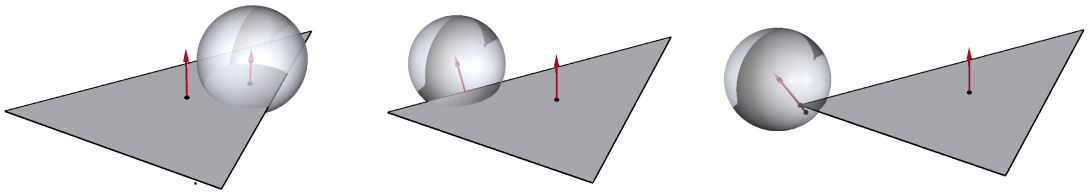

Figure 10: Three Contact Situations of Sphere - Triangle Intersection: Contact Point within Triangle Dimensions, Triangle Edge Intersection and Triangle Vertex Contact, respectively.

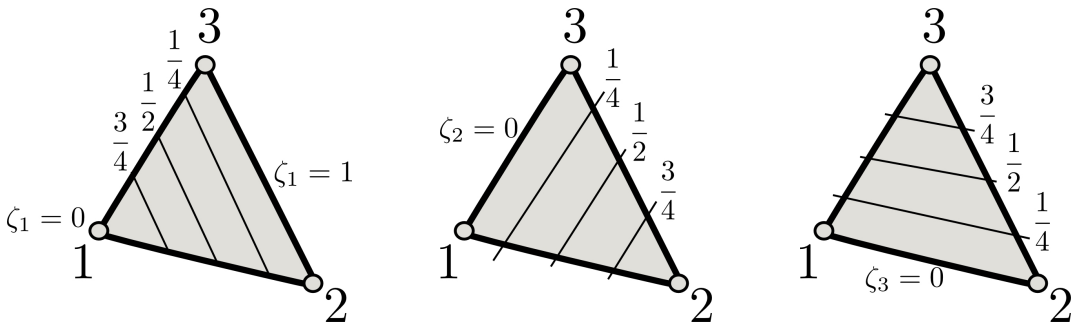

Figure 11: Constant lines of natural coordinates of a triangle.

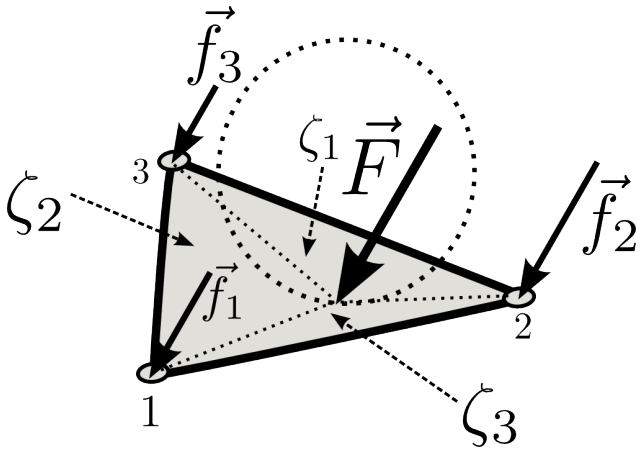

Figure 12: Particle force interpolated onto a linear triangle element.

forces for FEM. This equivalent states that the work of the particle force paired with the interpolated displacement equals the work achieved by the nodal forces and nodal displacement. Nakashima and Oida (2004) and Horner et al. (2001) used the same approach to couple DEM - FEM for analysing vehicle - soil and tire - soil interaction.

Looking at the contact situation in fig. 12, the finite element sees a point force acting on certain point of its surface. A point force can be written as the force multiplied by the Dirac functions. Eq. 36 represents the particle force $\vec{F}$ acting on the point $P(\zeta_1^P, \zeta_2^P, \zeta_3^P)$ of the triangle surface in natural coordinates.

$$F_j \cdot \delta(\zeta_1 - \zeta_1^P) \cdot \delta(\zeta_2 - \zeta_2^P) \cdot \delta(\zeta_3 - \zeta_3^P) \tag{36}$$

Let $\delta\vec{u}_n$ be the virtual node displacement and $\vec{f}_n$ the paired nodal force, then the left side term of eq. 38 represents the virtual work at the nodes. The right side term is the virtual work achieved by external forces.

$$\sum_n \delta W_n = \delta W_S \tag{37}$$

$$\sum_n \vec{f}_n \cdot \delta\vec{u}_n = \int_S \vec{f}_s \cdot \delta\vec{u}\, dS \tag{38}$$

$$\sum_n \vec{f_n} \cdot \delta\vec{u}_n = \int_S \vec{f_s} \cdot \left(\sum_n N_n \cdot \delta\vec{u}_n \right) dS$$

The interpolated virtual displacement for a linear triangle is described as follows:

$$\delta\vec{u} = N_1(\zeta_1) \cdot \delta\vec{u}_1 + N_2(\zeta_2) \cdot \delta\vec{u}_2 + N_3(\zeta_3) \cdot \delta\vec{u}_3$$

where N_1, N_2 and N_3 are the shape function of a three node finite element, i.e. linear triangle. Introducing this into eq. 38, where $\delta\vec{u}_n$ is the virtual nodal displacement and $N_n(\zeta_n) \cdot \delta\vec{u}_n$ its associated variation, and cancelling $\delta\vec{u}_n$ from both sides yields the following equation:

$$\vec{f_n} = \int_S \vec{f_s} \cdot N_n(\zeta_n)\, dS \tag{39}$$

Interpreting the surface integral by means of the natural coordinates and substitute the particle reaction force in eq. 39 by eq. 36 the following equation yields:

$$\vec{f_n} = \int_0^1 \vec{F} \cdot \delta(\zeta_n - \zeta_n^P) \cdot N_n(\zeta_n)\, d\zeta_n \tag{40}$$

$$\int_b^a Q(x) \cdot \delta(x - y)\, dx = Q(y) \quad \rightarrow \quad a \leq y \leq b \tag{41}$$

Using the integration law 41 of a Dirac function gives the distribution of the point forces $\vec{F}$ to the node force by means of the shape functions as formulated in eq. 42.

$$\left(\vec{f_n} = N_n(\zeta_n^P) \cdot \vec{F} \right)^e$$

$$\left(f_i^n = N_n(\zeta_n^P) \cdot F_i = \zeta_n^P \cdot F_i \right)^e \tag{42}$$

5. Simulation of Tire - Soil Interaction

The coupling approach between XDEM and FEM is employed to predict the tractive performance of a rubber tire in interaction with soil terrain. This allows to resolve the response of the rolling tire during the interaction with the terrain as well as the reaction of the soil bed on the tread. The simulation is set up according to the measurements of Shinone et al. (2010) for later comparisons with the numerical results.

5.1. Experimental Setup

The simulation is composed of two phases which are a phase of vertical tire sinkage followed by the horizontal travel of tire through the granular terrain by the angular velocity ω_t and translational velocity v_t. Fig. 13 depicts the two phases of tire travel schematically. During

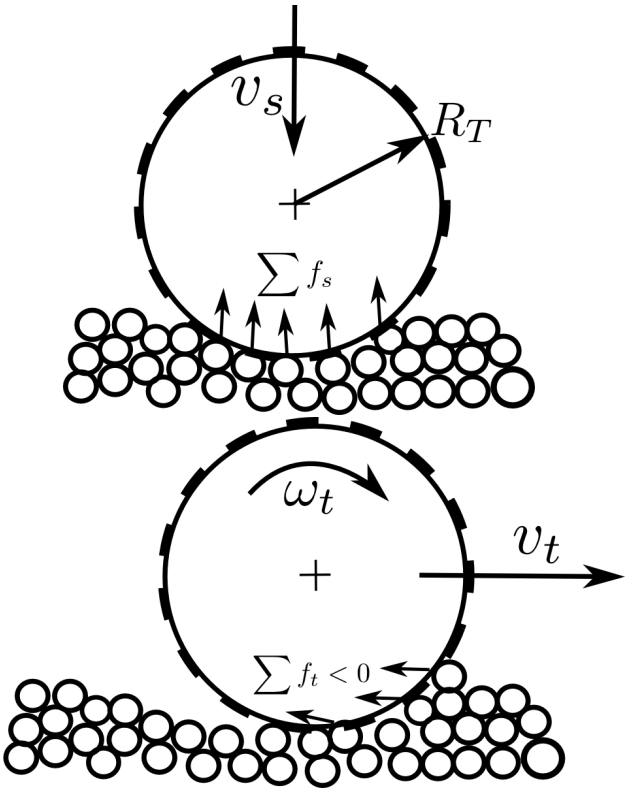

Figure 13: Sinkage and travel phase of tire - soil interaction

the sinkage phase the tire sinks into the soil bed under the constant velocity v_s until the contact force F_s is reached. F_s is thereby the sum of all vertical forces. Thereafter the tire travels through the soil bed in horizontal direction with a predefined tire slip s_T.

$$s_T = \frac{(\omega_t \cdot R_T - V_t)}{\omega_t \cdot R_T} \cdot 100 \quad [\%]$$

During the horizontal travel of the tire through the soil bed the the running resistance T_R, gross tractive effort T_H and drawbar pull T_P are recorded for later comparison with the experimental results. The running T_R resistance is predicted as the sum of all forces in opposite direction of travel which develop between the tire surface and grains in contact. This is indicated in fig. 13 and can be written as follows:

$$T_R = \sum f_t < 0$$

The gross tractive effort T_H as the the resistance counter part is thus predicted as:

$$T_H = \sum f_t > 0$$

Table 1: Tire Travel Properties Dimensions

Sinkage Velocity v_s [m/s]	0.1
Contact Force F_s [N]	5000
Horizontal Velocity v_t [m/s]	0.976
Angular Velocity ω_t [rad/s]	1.80
Tire Slip s_T [%]	5.0

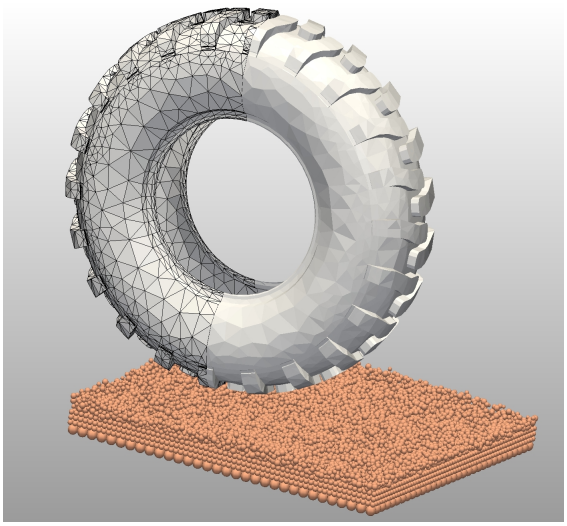

Figure 14: Initial soil bed and and tire configurations.

Finally the drawbar pull is calculated using the T_R and T_H as follows:

$$T_P = T_H - |T_R|$$

All properties describing the tire motion through the soil bed are composed in table 1. Fig. 14 shows the initial configuration of the meshed tire volume and the settled soil bed. The spatial dimensions of the tire tread and the soil bed are documented in table 2. Hence, the soil bed contains three layers of spherical particles of different radii which increasing with increasing soil bed height. Further, the top layer consists of particles with the smallest radius which have been randomly distributed and settled in a previous simulation to approximate a natural terrain environment. The bed is confined by rigid walls with the same material properties as the soil particles. Thus, the soil bed bottom is approximated as hard soil ground.
The tire tread consist of a lug pattern whereby the the

Table 2: Tire Tread and Soil Bed Dimensions

Tire size	$165/65R13$
Radius R_T [m]	0.544
Tread Width [m]	0.165
Wall Thickness [m]	0.016
Groove Depth [m]	0.015
Inflation Pressure [MPa]	0.14
No. Elements	24287

Bed Length [m]	1.0
Bed Width [m]	1.0
Bed Height [m]	~ 0.14
No. Grains	21812
Grain Diameter [mm]	15.6, 7.8, 6.9 $\pm$0.345

lugs are arranged in a alternating apposition. Further, the tire tread is approximate by tetrahedral finite elements with linear shape functions. However, the displacements at the nodes of the tire tread naturally contacting the rim are fixed. The inner surface of the tread experience the normal stress resulting from the inflation pressure.
The element of the outer surface of the tire tread are allowed to interact with soil grains according the described coupling procedure.
The deformation of the tire is predicted by the linear elastic finite element description and the soil bed motion is computed by the described discrete element method. Thus, the collision forces developing during the interaction between soil grains and between a soil grain and a tire element are predicted by the Hertz Mindlin model. The material properties used in the FEM, DEM and coupled prediction are stated in table 3.

5.2. Traction Performance and Deformation

Shinone et al. (2010) measured the drawbar pull and torque of lugged tire treads at different slip configurations. The investigations were conducted with a single-wheel tester composed of a soil bin and a driving unit of the tire. The tires measured had a similar nominal size as the simulated tire tread, i.e. $165/60R13$, with 535 mm diameter and 170 mm width. The measured

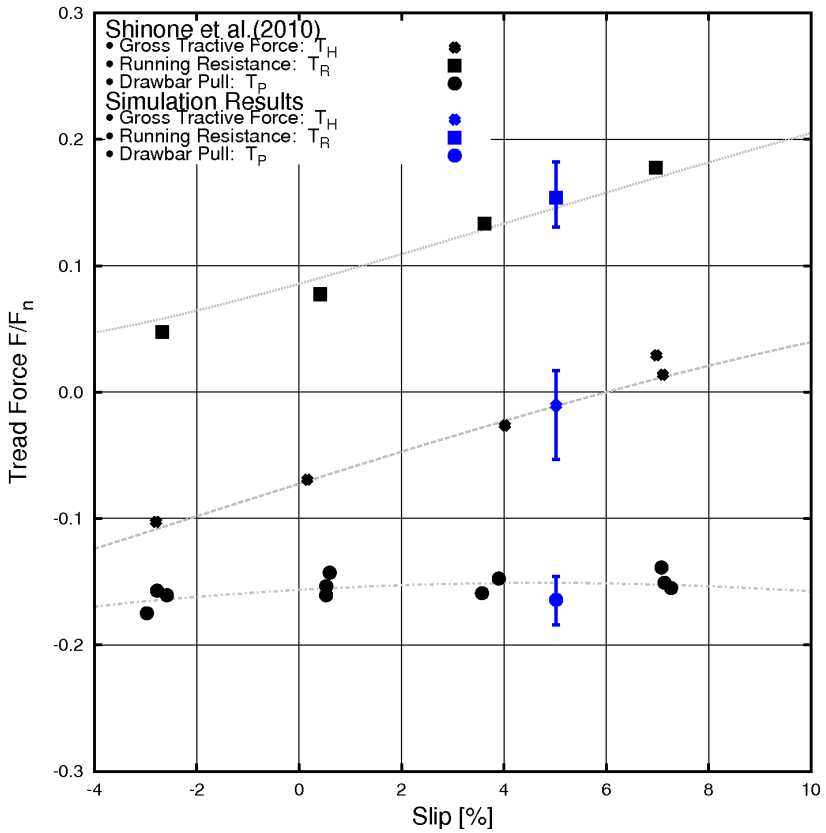

Figure 15: Gross Tractive Force, Running Resistance and Drawbar Pull versus tire slip. The black symbols indicate the measurements by Shinone et al. (2010) of lugged tire treads at different slip values. The blue symbols and error bars show the mean, min and max of the simulation results at a slip of 5%.

Table 3: Material and Contact Parameters

		Tread	Soil
Density	ρ [kg/m^3]	1100.0	2600.0
Young's Modulus	E [kPa]	20000.0	57.0
Poisson Ratio	ν	0.45	–
Shear Modulus	G [kPa]	–	4.0
Friction Coeff.	μ	0.3	0.6

torque of the tire was used to predict the gross tractive effort $T_H = M/R_T$. The running resistance R was then predicted from the difference of gross tractive effort and drawbar pull $|T_R| = T_H T_P$. The measurement results for lugged tire treads are shown as black symbols in fig. 15 at different slip values. Fig. 15 also contains the results of the coupled XDEM - FEM simulation at the slip value of 5.0%. The simulation results are shown as blue symbols of the mean value together with the min and max deviation. The overall traction performance has been predicted very successfully even though the tire mesh and soil resolution are rather coarse. This proofs the validity of the method for the application pf tire traction performance also in wake of this the dependence of the simulation properties should be investigated. Due to the interaction with tire tread the soil grains are compacted below and displaced onto the side of the tire which can be seen in fig. 16. Fig. 16 shows the tire from the backward position looking into the direction of travel. The soil grains are coloured by the velocity

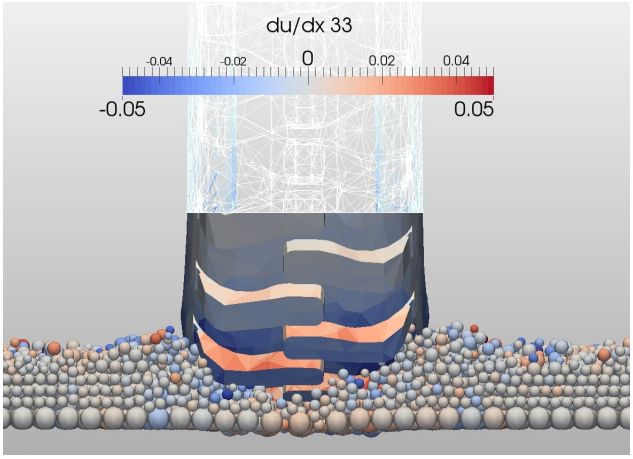

(a) Final sinkage position of the tire.

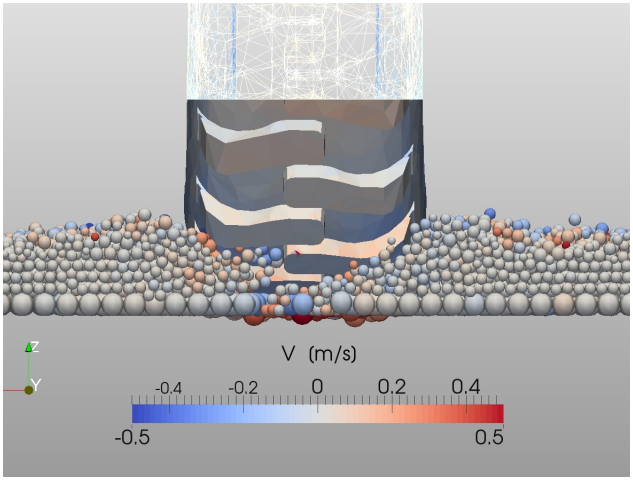

(b) The tire during travel through the soil bed.

Figure 16: Back view in travel direction of the tire during interaction with soil. The deformed tire coloured by the strain component ε_{33} of direction of sinkage. The soil grains are coloured by their velocity component in direction of travel.

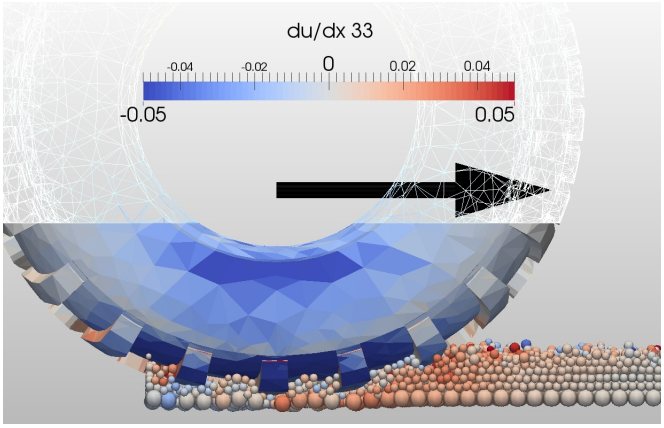

(a) Final sinkage position of the tire.

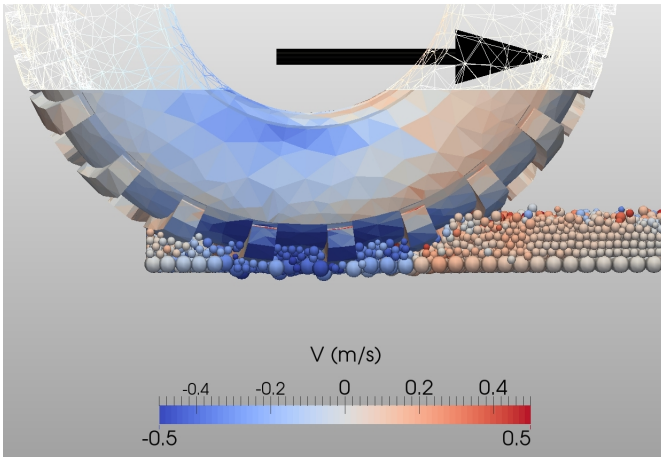

(b) The tire during travel through the soil bed.

Figure 17: Side view perpendicular to the travel direction of the tire during interaction with soil. The deformed tire is coloured by the strain component ε_{33} of direction of sinkage. The soil grains are coloured by their velocity component in direction of travel and the bed is depict clipped beneath the tread.

component in the direction of travel. Two progressing time steps are shown in fig. 16. The first depicts tire at the final sinkage position and the second whilst travel through the soil bed. The tire is represented in its deformed state and coloured by the strain component ε_{33} in sinkage direction. The displacement of the soil next to the tire is clearly visual as well as the deformation of the tire wall due to the interaction forces. Fig. 17 represents the same two timesteps shown in fig. 16 but in side view. The soil bed is thereby cut beneath the tire tread to allow an inside view. The colouring of the soil and tire is still by travel velocity and sinkage strain, respectively. This view visualizes clearly the maximum strain of the tire at the upper portion of the side wall due to the compression of the tread into the soil bed. Further, the acceleration of the soil grains beneath the the tread against the direction of travel is visual when one compares the two timesteps depict. The increase in velocity of the grains results from the grip of the tire into the bed whilst forward motion.

This grip of the footprint of the tire tread into soil bed is even more apparent in fig. 18. Fig. 18 shows a layer of the soil bed at the height of the tire lugs. With the motion of the tire into the direction of travel the majority of particles beneath the tread experiences an accelera-

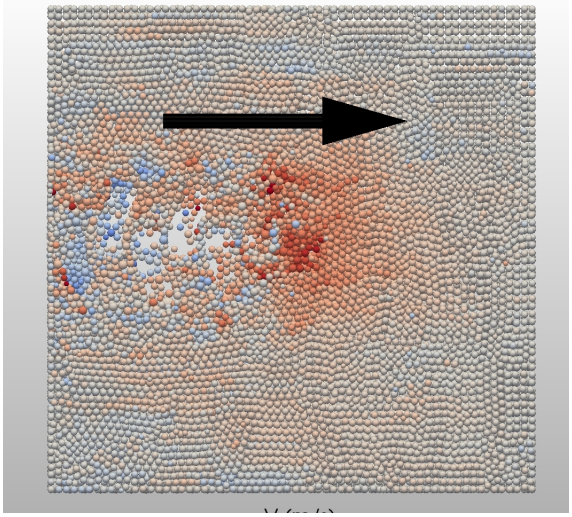

(a) Final sinkage position of the tire.

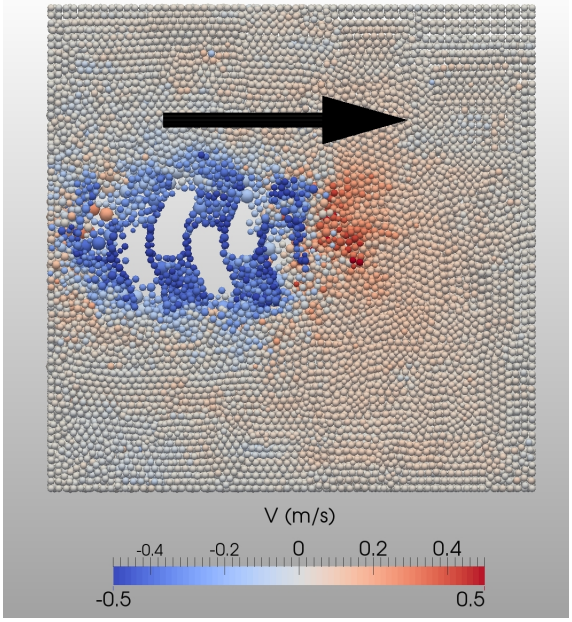

(b) The tire during travel through the soil bed.

Figure 18: Top view of soil bed during interaction with the tire. The soil grains are coloured by their velocity in direction of travel.

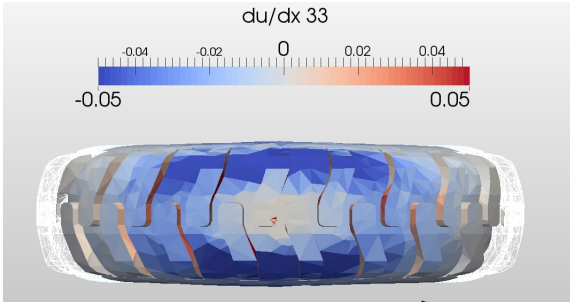

(a) Final sinkage position of the tire.

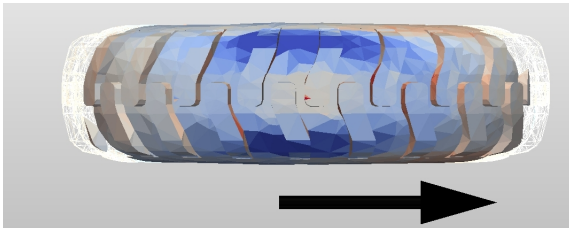

(b) The tire during travel through the soil bed.

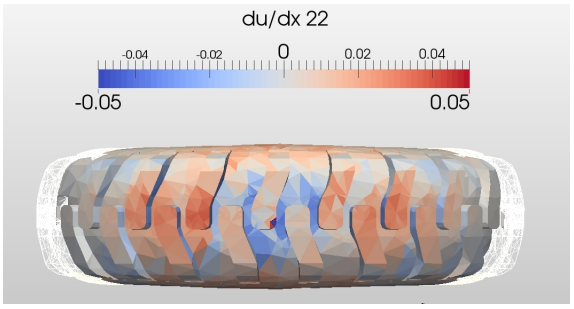

(c) Final sinkage position of the tire.

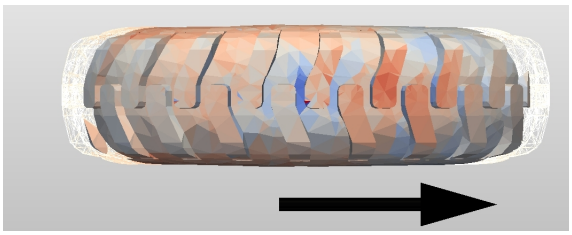

(d) The tire during travel through the soil bed.

Figure 19: Bottom view of the tire during interaction with soil. The deformed tire is depicted and coloured by the strain components ε_{22} of direction of travel and ε_{33} of direction of sinkage.

tion against the travel direction of tire under the applied slip. This portion of the particles cause the gross tractive effort predicted previously. A minor portion of the soil grains is pushed ahead of the tread. These grains develop forces against the travel direction of the tire and thus cause the running resistance. Also, under the rolling of the tire tread through the bed the lugged tread patterns are pressed into the soil due to the traction developed.

Fig. 19 depicts the bottom view of the tire tread at the same two timesteps. The strain component ε_{33} in direction of sinkage and the component ε_{22} in the direction of travel. The arrow in fig. 19 indicates the travel direction. Component ε_{33} indicates the maximum deformation on

the tread shoulder under the load pressure developed between tire and soil during sinkage. The first moment shows a symmetric distribution of the strain at the end of the sinkage phase. In component ε_{22} the maximum of the strain develops at the front part of the footprint due to the soil grains producing the running resistance.

6. Conclusions

A simulation technique has been developed and successfully applied to describe the interaction between a tire tread and a granular terrain. It supports the understanding of the nature of traction which consequently reveals measures to improve both traction and driving safety.

The Extended Discrete Element Method (XDEM) is employed to describe the mechanical behaviour of the soil. Contrary to a continuum mechanics approach soil is considered to exist of discrete grains are allowed to collide with each other. Therefore, a grain-scale contact models describes the interaction between the soil grains and the tire tread. The grain-scale response of each grain in contact with the tire surface is transferred to the tread by means of an interface coupling. Due to the response forces the tire tread develops deformations which are approached by a continuum description. Therefore, the tire tread itself is described by the Finite-Element-Method (FEM) which evaluates the elastic deformation due to contact forces of the terrain.

Hence, the following three key developments have been successfully conducted within this study: the continuous description of the tire tread; the DEM - FEM interface coupling; the discrete approach for the granular terrain;

The development of the DEM FEM interface meant to derive a coupling algorithm which enabled to connect the two domains efficiently. These developments first allowed the efficient detection of contact between the grains and the tread surface and also the transfer of forces and geometrical information between the DEM and FEM domain. The coupling algorithm connects the surface of the FEM mesh and its boundary surface in DEM. It further transfers the forces caused by the impacting grains onto the appropriate finite elements. Thereafter, it updates the boundary surface in DEM in accordance to the deformation predicted by the finite element solver. In order to describe the complex surface of a tire tread, the DEM software needed to be extended by a triangulated surface approximation. These triangular elements of the surface reflect the surface elements of a FEM mesh. A binary tree based algorithm has been developed and successfully employed for an efficient detection of contacts between the grains and the complex FEM surface.

However, the simulation technique proofed to be able to predict accurately the traction behaviour of tire tread -terrain interactions. The gross tractive effort, rolling resistance and draw-bar pull have been compared successfully to measurements by Shinone et al. (2010). The principal deformations of the tire tread and the granular terrain could be described by the DEM - FEM coupling method. However, the linear elastic description of the tire tread and the discretization as a whole rubber body are a first simple approach. For future works the tire model should be extended to non-linear deformations. The different layers and compounds of a modern high-tech tire have to be accounted in future predictions.

Acknowledgements

The presented research project is financed by the National Research Fund of Luxembourg (FNR). Simulations presented in this study were carried out using the High-Performance-Computing facility (HPC) of the University of Luxembourg, see HPC Varrette et al. (2014).

References

Beissel, S., Gerlach, C., Johnson, G., 2006. Hypervelocity impact computations with finite elements and meshfree particles. International Journal of Impact Engineering 33, 80–90. doi:10.1016/j.ijimpeng.2006.09.047. hypervelocity Impact Proceedings of the 2005 Symposium.

Hertz, H., 1881. Ueber die beruehrung elastischer koerper. Journal fr die reine und angewandte Mathematik 92, 156–171.

Horner, D.A., Peters, J.F., Carrillo, A., 2001. Large Scale Discrete Element Modeling of Vehicle-Soil Interaction. Journal of Engineering Mechanics 127(10), 1027–1032.

Idelsohn, S., Onate, E., Pin, F.D., Calvo, N., 2006. Fluid Structure Interaction Using the Particle Finite Element Method. International Center for Computational Methods in Engineering 195, 2100–2123.

Mindlin, R., 1949. Compliance of elastic bodies in contact. Applied Mechanics 16, 259–268.

Morris, J., Rubin, M., Block, G., Bonner, M., 2006. Simulations of fracture and fragmentation of geologic materials using combined FEM/DEM analysis. International Journal of Impact Engineering 33, 463–473. doi:10.1016/j.ijimpeng.2006.09.006. hypervelocity Impact Proceedings of the 2005 Symposium.

Nakashima, H., Oida, A., 2004. Algorithm and implementation of soil-tire contact analysis code based on dynamic FE-DE method. Journal of Terramechanics 41, 127–137.

Nakashima, H., Takatsu, Y., Shinone, H., Matsukawa, H., Kastani, T., 2009. FE-DEM Analysis of the Effect of Tread Pattern on the Tractive Performance of Tires Operating on Sand. Journal of Mechanical Systems for Transportation and Logistics 2, 55–65.

Nitka, M., Bilbie, G., Combe, G., Dascalu, C., Desrues, J., 2009. A DEM—FEM two scale approach of the behaviour of granular materials. AIP Conference Proceedings 1145, 443–446. doi:10.1063/1.3179957.

Samiei, K., 2012. Assessment of Implicit and Explicit Algorithms in Numerical Simulation of Granular Matter. Ph.D. thesis. University of Luxembourg.

Shinone, H., Nakashima, H., Takatsu, Y., Kasetani, T., Matsukawa, H., Shimizu, H., Miyasaka, J., Ohdoi, K., 2010. Experimental Analysis of Tread Pattern Effects on Tire Tractive Performance on Sand using an Indoor Traction Measurement System with Forced-slip Mechanism. EAEF 3 (2), 61–66.

Tsuji, Y., Kawaguchi, T., Tanaka, T., 1993. Discrete particle simulation of two-dimensional fluidized bed. Powder Technol. 77.

Tsuji, Y., Tanaka, T., Ishida, T., 1992. Lagrangian numerical simulation of plug flow of cohesionless particle in a horizontal pipe. Powder Technology 71, 239–250.

Varrette, S., Bouvry, P., Cartiaux, H., Georgatos, F., 2014. Management of an Academic HPC Cluster: The UL Experience, in: Proc. of the 2014 Intl. Conf. on High Performance Computing & Simulation (HPCS 2014), IEEE, Bologna, Italy.

Villard, P., Chevalier, B., Le Hello, B., Combe, G., 2009. Coupling between finite and discrete element methods for the modelling of earth structures reinforced by geosynthetic. Computers and Geotechnics 36, 709–717.

Xu, B.H., Yu, A.B., 1998. Comments on the paper numerical simulation of the gassolid flow in a fluidized bed by combining discrete particle method with computational fluid dynamics-reply. Chemical Engineering Science 53, 26462647.